

# TRIGONOMETRIC PARALLAXES TO STAR-FORMING REGIONS WITHIN 4 kpc OF THE GALACTIC CENTER

A. Sanna<sup>1</sup>, M. J. Reid<sup>2</sup>, K. M. Menten<sup>1</sup>, T. M. Dame<sup>2</sup>, B. Zhang<sup>1</sup>, M. Sato<sup>1</sup>, A. Brunthaler<sup>1</sup>, L. Moscadelli<sup>3</sup>, K. Immer<sup>1</sup>

asanna@mpifr-bonn.mpg.de

## ABSTRACT

We report four trigonometric parallaxes for high-mass star-forming regions within 4 kpc of the Galactic center. These measurements were made with the VLBA as part of the BeSSeL Survey. By associating these sources kinematically with large-scale features in CO and H I longitude-velocity diagrams, we begin to outline some major features of the inner Milky Way: the Connecting arm, the near and far 3 kpc arms, and the Norma arm. The Connecting arm in the first Galactic quadrant lies closer to the Galactic center than the far 3 kpc arm and is offset by the long-bar's major axis near its leading edge, supporting the presence of an inner Lindblad resonance. Assuming the 3 kpc arms are a continuous physical structure, the relative Galactocentric distance of its near and far sides suggests highly elliptical streamlines of gas around the bar(s) and a bar corotation radius,  $r_{\text{CR}} \gtrsim 3.6$  kpc. At a Galactic longitude near  $10^\circ$  and a heliocentric distance of about 5 kpc, the near 3 kpc arm and the Norma arm intersect on a face-on view of our Galaxy, while passing at different Galactic latitudes. We provide an accurate distance measurement to the W 31 star-forming complex of  $4.95^{+0.51}_{-0.43}$  kpc from the Sun, which associates it with a bright CO feature belonging to the near 3 kpc arm.

*Subject headings:* astrometry — Galaxy: fundamental parameters — Galaxy: kinematics and dynamics — masers — techniques: high angular resolution — stars: individual: W 31, G010.62–00.38, G010.47+00.02

---

<sup>1</sup>Max-Planck-Institut für Radioastronomie, Auf dem Hügel 69, 53121 Bonn, Germany

<sup>2</sup>Harvard-Smithsonian Center for Astrophysics, 60 Garden Street, Cambridge, MA 02138, USA

<sup>3</sup>INAF, Osservatorio Astrofisico di Arcetri, Largo E. Fermi 5, 50125 Firenze, Italy

## 1. Introduction

The so-called Galactic Molecular Ring (GMR) is a ridge of intense emission which dominates the appearance of extended CO gas in the longitude-velocity ( $\ell$ - $v$ ) diagram of our Galaxy (e.g., Dame et al. 2001). This prominent feature marks a region of enhanced molecular density roughly halfway between the Sun and the Galactic center, at Galactocentric radii ( $R$ ) between 4 and 6 kpc, which has been shown to likely trace gas emission from the inner spiral arms (e.g., Dobbs & Burkert 2012). Toward the Galactic center, the inner edge of the GMR would coincide with the Scutum-Centaurus arm, which we have recently located at an average Galactocentric radius of about 5 kpc (Sato et al., submitted.). Hereafter, we will refer to the region from the inner edge of the GMR to the Galactic center as the inner Milky Way.

As part of the Bar and Spiral Structure Legacy (BeSSeL) Survey <sup>1</sup>, we started a detailed study of the gas distribution and velocity field in the inner Milky Way, via trigonometric parallaxes and proper motions of masers in high-mass star-forming regions (HMSFRs). In this paper, we constrain some structures located in between the GMR and the Central Molecular Zone (CMZ; e.g., Morris & Serabyn 1996) in the first Galactic quadrant. These structures include the Connecting arm (e.g., Fux 1999; Marshall et al. 2008), the near and far 3 kpc arms (e.g., Dame & Thaddeus 2008), and the Norma arm as it is traced toward the Galactic center (e.g., Bronfman et al. 2000). The Connecting arm has received little discussion in the literature (e.g., Fux 1999 for a short summary; see also Rodriguez-Fernandez & Combes 2008, and references therein). It has been suggested to possibly appear similar to dust lanes observed in optical images of external galaxies along the extent of their bars, roughly *connecting* the nuclear ring with the inner tips of the spiral arms (e.g., see the Hubble Space Telescope composite view of the prototypical barred spiral galaxy NGC 1300, or that of NGC 1097). These dust lanes, often observed offset toward the leading edges of the bar structure in barred spirals, have been identified as tracers of shocks (e.g., Roberts et al. 1979; Athanassoula 1992b). In the following discussion, we will assume a general picture of the inner Galaxy as depicted in Churchwell et al. (2009), which accounts for the presence of two bar-like components: the boxy-bulge (i.e., the Galactic bar) and the long bar.

In this paper, we present trigonometric parallax measurements of 22 GHz H<sub>2</sub>O and 12 GHz CH<sub>3</sub>OH masers obtained with the Very Long Baseline Array (VLBA) for four sites of massive star formation located in the inner Galaxy.

---

<sup>1</sup>See the BeSSeL website at the following URL: <http://bessel.vlbi-astrometry.org/>

## 2. OBSERVATIONS

We conducted multi-epoch VLBA (program BR145)<sup>2</sup> observations of the  $6_{16} - 5_{23}$  H<sub>2</sub>O (rest frequency 22.235079 GHz) and the  $2_0 - 3_{-1}$ E CH<sub>3</sub>OH (rest frequency 12.178597 GHz) maser emission toward the four HMSFRs listed in Table 1. In order to measure trigonometric parallaxes and proper motions, we switched rapidly between a maser target and three or four extragalactic continuum sources. These calibrators were selected from our survey (Immer et al. 2011) and included ICRF sources (Fey et al. 2004) with accurate positions ( $\pm 2$  mas). We placed four geodetic-like blocks throughout each 7-hour track, in order to measure and remove atmospheric delays for each antenna. Details about the observational strategy can be found in Reid et al. (2009a, see also Sato et al. 2010). Observation and source information are summarized in Tables 1 and 2.

Four adjacent intermediate frequency (IF) bands, each 8 MHz wide, were recorded in dual circular polarization; each band was correlated to produce 256 spectral channels. The channel width of 31.25 kHz corresponds to a spectral resolution of 0.42 and 0.77 km s<sup>-1</sup> for the H<sub>2</sub>O and CH<sub>3</sub>OH maser transitions, respectively. The third IF band was centered about the LSR velocity ( $V_{\text{LSR}}$ ) of the strongest maser feature detected in our preparatory survey, as reported in Table 1 (under program BR145A). The data were processed with the VLBA DiFX software correlator in Socorro (Deller et al. 2007) using an averaging time of about 1 s, which limited the instantaneous field of view of the interferometer to about 3'' and 5'' for the H<sub>2</sub>O and CH<sub>3</sub>OH maser observations, respectively. Data were reduced with the NRAO Astronomical Image Processing System (AIPS) following the procedure described in Reid et al. (2009a), using a ParselTongue scripting interface (Kettenis et al. 2006). Total-power spectra of the 22.2 and 12.2 GHz maser emission toward G010.47+00.02, G010.62–00.38, G012.02–00.03, and G023.70–00.19 from the first epoch data are shown in Figure 1.

## 3. RESULTS

We modeled the position offsets of compact maser spots with respect to background sources as a function of time, in order to determine their parallaxes and proper motions (e.g., Reid et al. 2009a for details). During the fitting procedure, we quantified “a posteriori” the systematic errors, via error-floors added in quadrature to the formal fitting uncertainties, for the E–W and N–S offsets. These error floors were iteratively adjusted to yield values

---

<sup>2</sup>The VLBA is operated by the National Radio Astronomy Observatory (NRAO). The NRAO is a facility of the National Science Foundation operated under cooperative agreement by Associated Universities, Inc.

of chi-squared per degree of freedom near unity. Results of the parallax and proper motion fitting for each maser spot and QSO used are listed in Table 3 and displayed in Figures 2 to 5. For each source, individual parallax measurements with multiple maser spots and QSOs were combined in a final measurement and plotted in the right panel of Figure 2 to 5. The formal uncertainties of the combined fits were multiplied by  $\sqrt{N}$ , where  $N$  is the number of maser spots, to account for the possibility of correlated position shifts among the maser spots. Details on individual parallax fittings are presented in Appendix A. In Figure 6, the Galactic locations of our sources are superposed on a schematic face-on view of the Galaxy (re-scaled for a Sun-Galactic center distance of 8.38 kpc), with a number of spatial features updated from the recent literature, such as the position of the Galactic (e.g., Gerhard 2002) and long (Benjamin et al. 2005) bars as well as the streamline model of the 3 kpc arms by Green et al. (2011).

For each source, the line-of-sight velocity component ( $V_{\text{LSR}}$ ) and the eastward and northward motions on the plane of the sky ( $\mu_x, \mu_y$ ) give the 3-dimensional velocity vector of the star-forming region as measured with respect to the equatorial heliocentric reference frame (after adding the standard Solar motion to  $V_{\text{LSR}}$ ). In previous papers, to investigate deviations from a circular rotation about the Galactic center (i.e., the peculiar motion of the HMSFR), we have moved to a reference frame rotating with the Galaxy (e.g., Reid et al. 2009b). However, for sources with Galactocentric distances  $R < 4$  kpc, which may move along highly elliptical streamlines under the influence of the bulge/bar potential, we transform to a reference frame at rest at the Galactic center: ( $U_s^{\text{G.C.}}, V_s^{\text{G.C.}}, W_s^{\text{G.C.}}$ ).  $U_s^{\text{G.C.}}$ ,  $V_s^{\text{G.C.}}$ , and  $W_s^{\text{G.C.}}$  are directed toward the Galactic center, in the direction of Galactic rotation and toward the North Galactic Pole, respectively, at the location of each source<sup>3</sup>. In Table 4, we summarize our results together with those obtained for the other inner Galaxy sources in the literature. In this calculation, we adopted a current “best-estimate” of the Galactic parameters,  $R_0 = 8.38$  kpc and  $\Theta_0 = 243 \text{ km s}^{-1}$ , from the trigonometric parallaxes measured with maser lines (Reid 2013) and the revised *Hipparcos* measurements of the Solar motion from Schönrich et al. (2010).

---

<sup>3</sup>With respect to velocity components in a rotating reference frame ( $U_s, V_s, W_s$ ), the following relation holds:  $U_s^{\text{G.C.}} = U_s$ ,  $V_s^{\text{G.C.}} = V_s + \Theta(R)$ ,  $W_s^{\text{G.C.}} = W_s$ , where  $\Theta(R)$  gives the circular Galactic rotation at the source location (cf. Reid et al. 2009b).

### 3.1. Individual Sources

It is possible to associate each of the present HMSFRs to prominent large-scale features in CO and H I longitude-velocity diagrams of the inner Galaxy ( $|\ell| < 30^\circ$ ). In Figure 7, we present a longitude-velocity diagram of extended gas emission from the Galactic CO survey by Dame et al. (2001) with a number of structures relevant for discussing the inner few kpc of the Galactic center. The near and far 3 kpc arms appear as outlined by Dame & Thaddeus (2008), as parallel lanes within the range of longitudes where they can be followed clearly in CO ( $-12^\circ < \ell < +13^\circ$ ). Note that the far 3 kpc arm shows only weakly in Figure 7 (see Dame & Thaddeus 2008 for a detailed analysis). In the first quadrant, the line-of-sight velocity pattern of the near side of the Connecting arm, indicated in Figure 7 following the analysis by Fux (1999, e.g., his Figure 1 and Section 6.1), passes through the peak of the terminal velocity curve at positive longitudes. While crossing the  $\ell$ - $v$  pattern of the far 3 kpc arm at a Galactic longitude near  $10^\circ$ , this feature is better isolated at negative latitudes in both H I and CO (e.g., Figure 4 of Marshall et al. 2008). An approximate locus for the Norma/4 kpc arm in the  $\ell$ - $v$  diagram is obtained by assuming a logarithmic spiral with the following constraints: 1) an expanding motion fixed at  $\ell = 0^\circ$  of  $-29.3 \text{ km s}^{-1}$ , as obtained from CO spectra in absorption toward the Galactic center (first noticed by Kerr 1967 in H I; see also Greaves & Williams 1994 for CS absorption); 2) a southern tangent at a Galactic longitude of  $-32.5^\circ$  (e.g., Bronfman 2008, his Figure 2); 3) a northern tangent near  $25^\circ$  (e.g., Table 1 of Englmaier & Gerhard 1999, their “inner Scutum tangent”). The HMSFRs are not expected to follow the lines in Figure 7 to any better than the  $3\text{--}9 \text{ km s}^{-1}$  velocity dispersion of the molecular cloud population (e.g., Combes 1991, their Section 3.2.1). Similarly, velocity dispersions measured from hydrogen profiles show characteristic broadening by  $\sim 7 \text{ km s}^{-1}$ , that may be regarded as an upper limit due to the presence of blending features (e.g., Burton 1974).

In the following, we present our results for each source and list the associated arms in the last column of Table 4. Note that we also include two sources from previous measurements that are of interest for a general discussion (G009.62+00.19 and G023.44–00.18).

*G009.62+00.19.* According to Sanna et al. (2009), on the basis of a CO latitude-velocity analysis, this HMSFR is associated with gas along the Norma Arm at a distance of  $5.15_{-0.66}^{+0.77}$  kpc from the Sun, which corresponds to a Galactocentric radius of 3.4 kpc for  $R_0 = 8.38$  kpc. On the one hand, the near 3 kpc arm has an LSR velocity blueshifted by 15 to  $20 \text{ km s}^{-1}$  at the same longitude. The brightest CO emission from the near 3 kpc arm lies below the Galactic plane at Galactic longitudes greater than  $\approx 6^\circ$  and is offset by about  $0.5^\circ$  in latitude, with respect to the midplane of the Galaxy, at the Galactic longitude of the maser site (Figure 8; see also Figure 3 of Dame & Thaddeus 2008). On the other

hand, at  $\ell \approx 9.5^\circ$  the Norma arm peaks at velocities between 0-10  $\text{km s}^{-1}$  centered at about zero latitude, in agreement with the Galactic location and LSR velocity of G009.62+00.19 (Figure 8). We also note that the star-forming region appears to expand from the Galactic center at a velocity of about 36  $\text{km s}^{-1}$ , close to the Norma value of  $\approx 30 \text{ km s}^{-1}$  at zero longitude <sup>4</sup> (Table 4).

*G010.47+00.02.* At a parallax distance of  $8.55_{-0.55}^{+0.63}$  kpc from the Sun, our measurement translates to a Galactocentric radius of 1.6 kpc, assuming  $R_0 = 8.38$  kpc. The LSR velocity of large-scale emission associated with G010.47+00.02 ( $\sim 70 \text{ km s}^{-1}$ ) falls in the  $\ell$ - $v$  locus of the Connecting arm in the first quadrant, about 20  $\text{km s}^{-1}$  lower than a close by  $\ell$ - $v$  feature associated with the far 3 kpc arm (Figure 7). At the longitude of the source, the far 3 kpc arm shows a bump of faint emission below the Galactic plane (Figure 8; see also Figure 3 of Dame & Thaddeus 2008), whereas G010.47+00.02 lies close to zero latitude, a few tens of parsec above the Galactic plane. On the other hand, by comparing the velocity profile of the Connecting arm at  $\ell \sim 10.5^\circ$  with the latitude-velocity maps of Bitran et al. (1997, our Figure 8), one can clearly see a strong CO feature centered at zero latitude at the LSR velocity of G010.47+00.02. Therefore, we associate G010.47+00.02 with gas condensations belonging to the Connecting arm.

*G010.62–00.38.* The combined parallax measurement for G010.62–00.38 is  $0.202 \pm 0.019$  mas, which corresponds to a distance of  $4.95_{-0.43}^{+0.51}$  kpc from the Sun and a Galactocentric radius of 3.6 kpc (for  $R_0 = 8.38$  kpc). This prominent site of star formation has a combination of slightly negative LSR velocity ( $-3 \text{ km s}^{-1}$ ) and negative Galactic latitude, which associates the star-forming region with a bright CO feature belonging to the near 3 kpc arm (Figure 8, lower panel). In this range of longitudes, the Norma and near 3 kpc arms are clearly separated by about 20  $\text{km s}^{-1}$  at different distances below the Galactic plane (Figure 8). G010.62–00.38 belongs to the W31 star-forming complex that has been long thought to have an intrinsic, large, non-circular motion of several tens of  $\text{km s}^{-1}$ . While hydrogen recombination lines from the large-scale H II complex show velocities near zero, which could be associated with either nearby or very distant gas, absorption features from different molecules/transitions have been detected up to velocities of about 50  $\text{km s}^{-1}$  (see discussion in, e.g., Wilson 1974; Caswell et al. 1975; Fish et al. 2003). Along nearly circular orbits, the terminal velocity at  $\ell \approx 10^\circ$  would be in excess of three times the absorption cutoff assuming a IAU Galactic rotation speed, which would locate G010.62–00.38 on the near side of the tangent point

---

<sup>4</sup>In Table 4, we have assumed as the peak LSR velocity of the molecular cloud that from the CS(2–1) survey by Bronfman et al. (1996,  $+5 \text{ km s}^{-1}$ ), which is representative of the average velocity over the whole region. In Sanna et al. (2009), we assumed a slightly smaller velocity associated with the individual star-forming site G009.62+00.19 E.

(e.g., Fish et al. 2003, their Figure 1). While this argument has been questioned on the basis of a general deficiency of CO and H I gas within a Galactocentric radius of about 3 kpc (e.g., Figure 6 of Corbel & Eikenberry 2004), the current parallax distance of 5 kpc from the Sun indeed places W31 on the near edge of the Galactic gas hole, assuming the W31 cluster of H II regions is physically related (cf. Corbel & Eikenberry 2004, their Figure 8). The observed absorption cutoff is due to the radial expansion of G010.62–00.38 from the Galactic center ( $\sim 60 \text{ km s}^{-1}$ ), as inferred from its full-space kinematics (Table 4).

*G012.02–00.03.* We measured a combined trigonometric parallax of  $0.106 \pm 0.008$  mas for this source, corresponding to a distance of  $9.43_{-0.66}^{+0.77}$  kpc from the Sun and a Galactocentric radius of 2.1 kpc (for  $R_0 = 8.38$  kpc). In Figure 7, the  $\ell$ - $v$  position of G012.02–00.03 is associated with the locus of the far 3 kpc arm in the first Galactic quadrant, which lies close to zero latitude at the longitude of our source (Dame & Thaddeus 2008, their Figure 3). For  $\ell \approx 12^\circ$ , the current parallax measurement locates the far 3 kpc arm at almost half the distance to the Galactic center of the near 3 kpc arm at a similar longitudes (Figure 6), which has a direct implication for interpreting the nature of the 3 kpc feature of our Galaxy (see Section 4.1).

*G023.44–00.18.* Brunthaler et al. (2009) measured this massive star-forming region to be at a heliocentric distance of  $5.88_{-0.93}^{+1.37}$  kpc, or a Galactocentric radius of 3.8 kpc for  $R_0 = 8.38$  kpc, in the general direction of the northern Norma tangent in the first Galactic quadrant (Figure 7). According to Dame et al. (1986, their Figure 10b), at the longitude of the source, velocities in excess of  $+100 \text{ km s}^{-1}$  are expected for the inner regions of the Norma arm, whereas material in the Scutum arm would show LSR velocities which are more than  $30 \text{ km s}^{-1}$  below that of G023.44–00.18. Therefore, we associate G023.44–00.18 as belonging to the Norma arm near its tangent.

*G023.70–00.19.* The distance to this star formation site is  $6.21_{-0.80}^{+1.0}$  kpc, which corresponds to a Galactocentric radius of 3.7 kpc (for  $R_0 = 8.38$  kpc). This measurement locates G023.70–00.19 only a few hundred pc away from G023.44–00.18 in a similar direction below the Galactic plane, which argues for an association with the Norma arm. As shown in Figure 7, its LSR velocity of about  $+77 \text{ km s}^{-1}$  associates the star-forming region to gas emission at the low-longitude edge of a “gas hole” near  $\ell \sim 25^\circ$ . According to Cohen et al. (1980, their Figure 2), molecular gas at velocities between  $70$ – $90 \text{ km s}^{-1}$  and Galactic longitudes between  $23^\circ$  and  $25^\circ$  is associated with the Norma arm. At a similar longitude, gas belonging to the nearby Scutum arm shows LSR velocities less than  $+60 \text{ km s}^{-1}$  that involves CO emission below the gas hole. Therefore, we associate G023.70–00.19 with gas condensations in the Norma arm.

#### 4. Discussion

Together with the two previous measurements listed in Table 4, the HMSFRs presented here sample the inner regions of the Milky Way at Galactic longitudes from  $+9.6^\circ$  to  $+23.7^\circ$  and Galactocentric radii between 1.6 and 3.8 kpc. In the inner Galaxy, the mass distribution of the Galactic (nested) bar(s) provides non-axisymmetric gravitational perturbations on gas and stellar orbits, whereas a nearly flat rotation curve is generally measured between Galactocentric radii of about 4 to 13 kpc (e.g., Reid et al. 2009b, Honma et al. 2012). Under the influence of a bar potential, highly non-circular streamlines of gas and stellar orbits are indeed expected as for the families of periodic orbits,  $x_1$ ,  $x_2$ , and  $x_3$  (e.g., Contopoulos & Papayannopoulos 1980; van Albada & Sanders 1982; Athanassoula 1992a); these streamlines would appear on  $\ell - v$  diagrams as parallelogram-shaped features (e.g., Binney et al. 1991; Bureau & Athanassoula 1999). A comparison of the measured LSR velocities with those expected for circular orbits (e.g., Englmaier & Gerhard 1999) at the longitudes and Galactocentric distances of our sample shows, in general, differences of several tens of  $\text{km s}^{-1}$  (e.g., Sanna et al. 2009). From Table 4, a weighted average of the rotation speed of HMSFRs in the inner Milky Way differs by about  $-40 \pm 5 \text{ km s}^{-1}$  from the rotation speed at the Solar circle of  $\Theta_0 = 243 \text{ km s}^{-1}$  (Reid 2013). This value is significantly lower than the average peculiar motion derived for HMSFRs at Galactocentric radii greater than 4 kpc, which lag Galactic rotation by less than  $10 \text{ km s}^{-1}$  (e.g., Xu et al. 2013). We note that this result does not depend sensitively on the value of  $\Theta_0$  assumed in the calculation. Evidence for a substantially flat rotation curve which drops inwards at small Galactocentric radii are commonly observed for barred galaxies with rotation velocities comparable to the Milky Way (e.g., Sofue et al. 1999).

Moving from the star-forming region closest to the Galactic center (G010.47+00.02) to the one farthest from the center (G023.44–00.18), we start to fix the positions of the major arm-like features of the inner Milky Way on a coherent face-on view (Figure 6). In the following, we describe these constraints in brief. Within about 3 kpc of the Galactic center and outside the CMZ, three CO features pointed out on the  $\ell$ - $v$  diagram of Figure 7 dominate the gas kinematics, the near and far 3 kpc arms (yellow lines) and the Connecting arm (green line). The Connecting arm, as fixed by the position of G010.47+00.02 at  $R = 1.6_{-0.1}^{+0.2}$  kpc, apparently runs along the far edge of the long bar, probably closer to the Galactic center than the far 3 kpc arm, constrained at a similar longitude by the position of G012.02–00.03 at  $R = 2.1_{-0.3}^{+0.5}$  kpc. The distance measurement to G010.62–00.38 further constrains the position of the near side of the 3 kpc arm at a Galactocentric radius ( $R = 3.6_{-0.4}^{+0.4}$  kpc) almost twice that of G012.02–00.03. Despite early claims that the near 3 kpc arm was deficient in star formation activity (e.g., Lockman 1980), at the position of our sources the CO velocity-integrated maps show local peaks of emission (Figure 3 of Dame & Thaddeus 2008), which



pinpoint enhanced star formation such as in the prominent W31 complex. This is also in agreement with the recent detection of several, massive, star formation sites from the Methanol Multibeam Survey that are associated in longitude, latitude, and velocity with the brightest CO emission along the 3 kpc arms (cf. Figure 2 of Green et al. 2009 and Figure 3 of Dame & Thaddeus 2008).

In the first Galactic quadrant, outward of 3 kpc from the Galactic center but within the GMR, an annulus of less than 2 kpc in radius encompasses the northern Scutum-Centaurus, Norma, and near 3 kpc arm tangents (Figure 6). This is evident, for instance, in the Galactic Ring Survey of extended  $^{13}\text{CO}$  emission along the Galactic plane, with prominent concentrations at  $\ell \sim 31^\circ$  and  $23^\circ$  (Jackson et al. 2006, their Figure 1). While interarm distances are expected to decrease as the arms converge to the end of the (long) bar at a Galactocentric azimuth near  $45^\circ$  (i.e., the angle between the Sun and the source as viewed from the Galactic center,  $\beta$ ), our distance measurements for G009.62+00.19 and G010.62–00.38 show that the Norma and near 3 kpc arms nearly overlap at a Galactic longitude of  $10^\circ$  ( $\beta \sim 14^\circ$ ) on a face-on view of the Milky Way (Figure 6). On the other hand, a  $b$ - $v$  analysis of the CO emission from the arms at this longitude reveals that their gas distributions do not mix, with the near 3 kpc arm passing under (at lower Galactic latitudes) the Norma arm (Figure 8).

#### 4.1. Topics on the Inner Arm Features

The small number of measured distances to sources in the inner portion of the Galaxy precludes a thorough discussion on individual arm features at this time. Similarly, an analysis of the inner rotation curve ( $R < 4$  kpc), which one would expect to have a strong azimuthal dependence, is also premature. However, our measurements still allow us to start discussing two specific topics.

Firstly, if the star-forming region G010.47+00.02 is located in the Connecting arm at a longitude of  $\ell \sim 10.5^\circ$ , then it is close to the far edge of both the Galactic and “long” bars in the first Galactic quadrant (Figure 6). According to Roberts et al. (1979, their Section 4), streamlines of gas crossing the major axis of a bar strongly decelerate near their maximum radial excursion, where gas approaches a potential minimum (e.g., Figure 5 and 6 of Roberts et al. 1979). A major effect of slowing down abruptly would be that gas piles up until a shock occurs (i.e., the locus of the Connecting arm). We find for G010.47+00.02 that the  $V_s^{\text{G.C.}}$  velocity component of  $122 \pm 16 \text{ km s}^{-1}$  (in the direction of Galactic rotation) is slower by almost a factor of 2 than the circular rotation speed beyond 4 kpc in the Galaxy. While the rotation curve is expected to drop toward the center owing to less mass enclosed, a nearby HMSFR belonging to the far 3 kpc arm (G012.02–00.03) shows a rotation

speed of  $215 \pm 27 \text{ km s}^{-1}$ . This evidence suggests that the  $V_s^{\text{G.C.}}$  value of G010.47+00.02 is likely related to the local gas dynamics, and represents an argument in favor of the shock phenomenon as the origin of its peculiar motion. The position of the Connecting arm with respect to the axis of the bar(s), and the direction of the gas flow along the Connecting arm itself ( $U_s^{\text{G.C.}}$  component in Table 4), should be intimately related to the presence of an inner Lindblad resonance (ILR) close to the Galactic center (e.g., Roberts et al. 1979; Athanassoula 1992b; Athanassoula & Bureau 1999). If an ILR is present, or equivalently if the  $x_2$  family of stable periodic orbits exist (i.e., orbits oriented perpendicular to the bar major axis), the shock locus should be offset toward the leading edge of the bar; the larger the  $x_2$  orbit along the bar minor axis, the bigger will be the offset of the Connecting arm with respect to the major axis of the bar (e.g., Figure 5 of Athanassoula 1992b). The position of G010.47+00.02 is offset by about 1.3 kpc (i.e.,  $\approx 2\sigma$ ) from the direction of the major axis of the long bar. While we cannot rule out an overestimate of our distance measurement by  $2\sigma$ , the current measurement supports the Connecting arm being shifted forward (clockwise in phase) toward the far side of the bar in the first Galactic quadrant, or alternatively it supports the presence of an ILR. Roberts et al. (1979, their Figure 6) also predict that a shock-focusing phenomenon should develop where an ILR is present. Given that, forced by the ILR, the Connecting arm would be inclined with respect to the orientation of the bar’s major axis, then streamlines of gas at different Galactocentric radii would enter the shock front at different angles. As a result, gas along the Connecting arm in the outer bar regions would have a net inward motion toward the Galactic center with velocities of some tens of  $\text{km s}^{-1}$ ; at some Galactocentric radii inwards, the gas motion along the shocked layer would invert direction, showing an instantaneous velocity component outward from the Galactic center with velocities of the order of  $100 \text{ km s}^{-1}$ . The overall effect of the shock-focusing phenomenon would be to channel gas at some Galactocentric radii and enhanced star formation activity would be expected in the region of converging flows. According to Roberts et al. (1979), a detection of an outward motion along the Connecting arm would be an independent confirmation for the presence of an ILR in the bar region. Our data show a combination of offset shock and inward motion that would confine the shock-focusing phenomenon (if present) to Galactocentric radii within about 1.6 kpc from the Galactic center.

A second topic concerns the nature of the near and far 3 kpc arms (e.g., see the review in Section 3.2 of Green et al. 2011). We follow the interpretation of the 3 kpc arms as a continuous physical structure as opposed to, for instance, a combination of two, separate, lateral arms. This assumption is based on a better match of the former interpretation to the  $\ell$ - $v$  locus of the 3 kpc arm features (cf. Figure 7, 10, and 11 in Green et al. 2011). In this context, two main ideas have been forwarded: 1) that of a circular ring with an

expanding motion away from the Galactic center (e.g., van der Kruit 1971), and 2) that of an elliptical streamline of gas around the bar region (e.g., Peters 1975). An important difference between the two models is related to the position of the 3 kpc arm with respect to the radius of the corotation resonance ( $r_{\text{CR}}$ , associated with the rotation pattern of the bars): elliptical orbits are expected inside  $r_{\text{CR}}$ , whereas nearly circular orbits should occur outside (e.g., Contopoulos & Papayannopoulos 1980). The Galactocentric radius of the near 3 kpc arm at the position of G010.62–00.38 ( $R = 3.6_{-0.4}^{+0.4}$  kpc) is almost two times greater than the Galactocentric radius of the far 3 kpc arm, as inferred from the position of G012.02–00.03 ( $R = 2.1_{-0.3}^{+0.5}$  kpc). This does not match the expected constant radius for a circular ring and seems to favor a highly eccentric orbit. If the interpretation of elliptical orbits holds, we also note that the maximum Galactocentric radius measured for the 3 kpc arms (for G010.62–00.38) provides a lower limit to the radius of corotation at  $r_{\text{CR}} \gtrsim 3.6$  kpc, consistent with previous findings from the literature (e.g., Englmaier & Gerhard 1999, their Section 4.5).

In Figure 6, the elliptical model by Green et al. (2011) for the 3 kpc feature provides a good match to the position of the two HMSFRs. This model assumes that gas belonging to the 3 kpc arms flows along an elliptical streamline and has a constant angular momentum at any given point of the ellipse, with a value of  $320 \text{ km s}^{-1} \text{ kpc}$ . Locally, the tangential velocity is given by the ratio of the angular momentum and the Galactocentric radius at that point. Our measured proper motions for G010.62–00.38 and G012.02–00.03 give values of the angular momentum higher than  $400 \text{ km s}^{-1} \text{ kpc}$ . By increasing the angular momentum value, the model by Green et al. still provides a reasonable fit to the data, but requires a shift of the ellipse orientation at smaller angles with respect to the Sun-Galactic center direction (e.g., Figure 8 of Green et al. 2011). Whether or not the orientation of the ellipse fits better the direction of the long ( $\beta \sim 45^\circ$ ) or the Galactic bar ( $\beta \sim 20^\circ$ ) would be a hint as to which bar component dominates the gas response. While our data still do not constrain the ellipse orientation with sufficient accuracy, we should be able to assess these issues with stronger statistical support when more parallax measurements in the inner Milky Way will be available.

This work was partially funded by the ERC Advanced Investigator Grant GLOSTAR (247078). This work made use of the Swinburne University of Technology software correlator, developed as part of the Australian Major National Research Facilities Programme and operated under licence.

*Facilities:* VLBA.

### A. Parallax and Proper Motion Fitting Details

Maser spots for parallax fitting were selected according to the following criteria: 1) spots persisting over one year that belong to isolated features, in order to avoid emission blended between different maser centers; 2) compact maser spots, unresolved by the VLBA beam or slightly resolved but with a stable, deconvolved, position angle; 3) strong maser spots ( $\sim 1 - 10 \text{ Jy beam}^{-1}$ ) with typical signal-to-noise ratios of more than a hundred.

*G010.62–00.38*. For the purposes of a maser reference position, we employed three spots at the LSR velocities of  $-14.2$ ,  $-1.1$ , and  $+1.0 \text{ km s}^{-1}$  from the  $\text{H}_2\text{O}$  maser distribution measured within the field of view of the VLBA. Among the calibrators observed in K band, the two stronger QSOs in Table 2, J1821–2110 and J1751–1950, served as a background reference position and their images from the first epoch data are shown in Figure 9. The angular separation on the plane of the sky ( $\theta_{\text{sep}}$ ) between the background QSOs and the target maser is reported in Table 2. The ICRF J1751–1950 was detected at each epoch above a  $5\sigma$  level; at the third epoch, the peak intensity of J1821–2110 fell below a  $3\sigma$  level due to poor phase stability between the maser and the calibrator (because of poor weather conditions) and was not used. Due to the lack of the third epoch data, parallax fitting with the calibrator J1821–2110 results in a higher correlation between the parallax sinusoid and the (linear) proper motion component from each maser spot. Since we expect no detectable proper motion for the extragalactic sources, parallax fitting with J1821–2110 was constrained with proper motions determined from J1751–1950 for each spot. The error-floors determined by combining the measurements of the three maser spots with respect to the two QSOs were  $\pm 0.05 \text{ mas}$  in the E–W direction and  $\pm 0.07 \text{ mas}$  in the N–S direction. Since water maser cloudlets have typical proper motions of tens of  $\text{km s}^{-1}$ , determining a secular proper motion for the HMSFR requires to correct for maser velocity components. We estimated this contribution from the average proper motion of all maser features (80) determined as in Sanna et al. (2010) with respect to the reference spot at  $+1.1 \text{ km s}^{-1}$ , used for the parallax fitting and with the more accurate proper motion measurement. The average, internal, velocity components are  $-0.01 \pm 0.03 \text{ mas yr}^{-1}$  toward the east and  $+0.28 \pm 0.02 \text{ mas yr}^{-1}$  toward the north, where we report the standard error of the mean. Thus, the secular proper motion of the HMSFR is estimated to be  $-0.366 \pm 0.081 \text{ mas yr}^{-1}$  and  $-0.600 \pm 0.055 \text{ mas yr}^{-1}$  in the east and north directions, respectively. We explicitly note that these small uncertainties may still be affected by a further uncertainty of several tenth of  $\text{mas yr}^{-1}$ , due to the complexity of *G010.62–00.38* as a cluster of young stellar objects (e.g., Liu et al. 2011). At our measured distance, these values correspond to  $-8.6 \pm 1.9 \text{ km s}^{-1}$  and  $-14.1 \pm 1.3 \text{ km s}^{-1}$  eastward and northward, respectively. Completing the kinematic information, we assume an LSR velocity of  $-3.0 \pm 2.7 \text{ km s}^{-1}$  for the HMSFR *G010.62–00.38*, obtained from the large-scale rest velocity of the CS (1–0) and  $\text{NH}_3$  (1,1) line emission (Anglada et al.

1996).

*G010.47+00.02.* As a maser reference position, we combined the positions of seven spots associated with seven distinct maser cloudlets spread over a region of about 0.4 arcsec in size (Table 3). Imaging of the calibrators for G010.47+00.02 was optimized by setting an elevation cutoff of  $25^\circ$  for each antenna. Among the set of calibrators observed in combination with G010.47+00.02, only the ICRF calibrator J1751–1950, at an angular offset of  $3^\circ$  from the target maser (Table 2), had a distinct peak of emission at all epochs and has been used as a background reference position in the parallax measurement (Figure 9). The error-floors determined from the simultaneous fitting of these seven maser spots were  $\pm 0.01$  mas and  $\pm 0.09$  mas toward the E–W and N–S directions, respectively. As for G010.62–00.38, we estimated the secular proper motion of the star-forming region by subtracting the relative motion of all measured maser features (11) with respect to the reference spot at  $+68.0 \text{ km s}^{-1}$  (Table 3). The average internal velocity components are  $+0.073 \pm 0.006 \text{ mas yr}^{-1}$  toward the east and  $-0.22 \pm 0.08 \text{ mas yr}^{-1}$  toward the north, where we report the standard error of the mean. Thus, the total motion of the whole source is estimated to be  $-3.860 \pm 0.015 \text{ mas yr}^{-1}$  and  $-6.403 \pm 0.076 \text{ mas yr}^{-1}$  in the east and north directions, respectively. At our measured distance, these values correspond to  $-156.4 \pm 0.6 \text{ km s}^{-1}$  and  $-259.5 \pm 3.1 \text{ km s}^{-1}$  eastward and northward, respectively.

*G012.02–00.03.* The 12.2 GHz methanol maser from G012.02–00.03 consists of a single spectral feature persisting during the four observing epochs with emission extended over an area of a few mas (squared). The brightness distribution is centrally peaked and we employed the peak positions of two velocity channels, at  $+108.0$  and  $+108.8 \text{ km s}^{-1}$ , as maser reference positions. While the U-band calibrators were easily detected at all epochs, only the closer QSO J1808–1822 (see Table 2) had a stable spatial morphology (deconvolved size) suitable for an accurate parallax measurement. The error-floors from these combined measurements were  $\pm 0.01$  mas and  $\pm 0.19$  mas toward the E–W and N–S directions, respectively. Methanol masers move with typical velocities of only a few  $\text{km s}^{-1}$  that are very close to the systemic velocity of the molecular cloud core they are associated with. Therefore, we will neglect their contribution for computing the secular proper motion of G012.02–00.03. By averaging the proper motion inferred from the two maser spots, we obtain Galactic velocity components of  $-183.6 \pm 1.0 \text{ km s}^{-1}$  and  $-346.7 \pm 11.8 \text{ km s}^{-1}$  eastward and northward, respectively.

*G023.70–0.19.* For the parallax measurement of G023.70–00.19 we made use of three maser spots, two of them are associated with the peak position of the 12.2 GHz methanol maser emission (at  $+77.5$  and  $+79.0 \text{ km s}^{-1}$ ) and a third spot is associated with an isolated maser cloudlets at about 21 mas to the south of the peak emission (at  $+76.7 \text{ km s}^{-1}$ ). Only measurements with the two closer calibrators (see Table 2), J1825–0737 and J1846–0651,

gave individual error-floors in the E-W direction smaller than 0.1 mas for each maser spot and were used in the parallax estimate. These final error-floors were  $\pm 0.06$  mas and  $\pm 0.15$  mas toward the E–W and N–S directions, respectively. By averaging the proper motion inferred from the three maser spots, we obtain Galactic velocity components of  $-94.4 \pm 2.0$  km s $^{-1}$  and  $-187.4 \pm 4.0$  km s $^{-1}$  eastward and northward, respectively. Toward the maser position, CS (2–1) line emission shows an LSR velocity of  $+68.3$  km s $^{-1}$  (Bronfman et al. 1996), about ten km s $^{-1}$  slower than the peak velocity of the H110 $\alpha$  line at the same position (Sewilo et al. 2004,  $+76.5$  km s $^{-1}$ ). In order to resolve the near/far kinematic distance ambiguity, Sewilo et al. observed the H<sub>2</sub>CO (1<sub>10</sub>–1<sub>11</sub>) line in absorption against the H II region up to velocities of  $+86$  km s $^{-1}$ , with an H<sub>2</sub>CO absorption component at the same velocity of the CS line. Following these evidence, we assume a central LSR velocity for the HMSFR G023.70–00.19 of  $+76.5 \pm 10$  km s $^{-1}$ , that better matches the 12 GHz CH<sub>3</sub>OH maser velocities of Figure 1, which usually trace more quiescent gas dynamics close to the systemic velocity of the region ( $< 5 - 10$  km s $^{-1}$ ).

## REFERENCES

- Anglada, G., Estalella, R., Pastor, J., Rodriguez, L. F., & Haschick, A. D. 1996, ApJ, 463, 205
- Athanassoula, E., & Bureau, M. 1999, ApJ, 522, 699
- Athanassoula, E. 1992, MNRAS, 259, 328
- Athanassoula, E. 1992, MNRAS, 259, 345
- Benjamin, R. A., et al. 2005, ApJ, 630, L149
- Beuther, H., Schilke, P., Menten, K. M., et al. 2002, ApJ, 566, 945
- Binney, J., Gerhard, O. E., Stark, A. A., Bally, J., & Uchida, K. I. 1991, MNRAS, 252, 210
- Bitran, M., Alvarez, H., Bronfman, L., May, J., & Thaddeus, P. 1997, A&AS, 125, 99
- Bronfman, L., Nyman, L.-A., & May, J. 1996, A&AS, 115, 81
- Bronfman, L., Casassus, S., May, J., & Nyman, L.-Å. 2000, A&A, 358, 521
- Bronfman, L. 2008, Ap&SS, 313, 81
- Brunthaler, A., Reid, M. J., Menten, K. M., et al. 2009, ApJ, 693, 424

- Bureau, M., & Athanassoula, E. 1999, *ApJ*, 522, 686
- Burton, W. B. 1974, *Galactic Radio Astronomy*, 60, 551
- Caswell, J. L., Murray, J. D., Roger, R. S., Cole, D. J., & Cooke, D. J. 1975, *A&A*, 45, 239
- Churchwell, E., Babler, B. L., Meade, M. R., et al. 2009, *PASP*, 121, 213
- Clemens, D. P., Sanders, D. B., & Scoville, N. Z. 1988, *ApJ*, 327, 139
- Cohen, R. J., & Davies, R. D. 1976, *MNRAS*, 175, 1
- Cohen, R. S., Cong, H., Dame, T. M., & Thaddeus, P. 1980, *ApJ*, 239, L53
- Combes, F. 1991, *ARA&A*, 29, 195
- Contopoulos, G., & Papayannopoulos, T. 1980, *A&A*, 92, 33
- Corbel, S., & Eikenberry, S. S. 2004, *A&A*, 419, 191
- Dame, T. M., Elmegreen, B. G., Cohen, R. S., & Thaddeus, P. 1986, *ApJ*, 305, 892
- Dame, T. M., Hartmann, D., & Thaddeus, P. 2001, *ApJ*, 547, 792
- Dame, T. M., & Thaddeus, P. 2008, *ApJ*, 683, L143
- Dame, T. M., & Thaddeus, P. 2011, *ApJ*, 734, L24
- Deller, A. T., Tingay, S. J., Bailes, M., & West, C. 2007, *PASP*, 119, 318
- Dobbs, C. L., & Burkert, A. 2012, *MNRAS*, 421, 2940
- Downes, D., Wilson, T. L., Bieging, J., & Wink, J. 1980, *A&AS*, 40, 379
- Englmaier, P., & Gerhard, O. 1999, *MNRAS*, 304, 512
- Fey, A. L., Ma, C., Arias, E. F., et al. 2004, *AJ*, 127, 3587
- Fish, V. L., Reid, M. J., Wilner, D. J., & Churchwell, E. 2003, *ApJ*, 587, 701
- Fux, R. 1999, *A&A*, 345, 787
- Gerhard, O. 2002, *The Dynamics, Structure & History of Galaxies: A Workshop in Honour of Professor Ken Freeman*, 273, 73
- Greaves, J. S., & Williams, P. G. 1994, *A&A*, 290, 259

- Green, J. A., McClure-Griffiths, N. M., Caswell, J. L., et al. 2009, *ApJ*, 696, L156
- Green, J. A., Caswell, J. L., McClure-Griffiths, N. M., et al. 2011, *ApJ*, 733, 27
- Hofner, P., & Churchwell, E. 1996, *A&AS*, 120, 283
- Honma, M., Nagayama, T., Ando, K., et al. 2012, *PASJ*, 64, 136
- Hou, L. G., Han, J. L., & Shi, W. B. 2009, *A&A*, 499, 473
- Immer, K., Brunthaler, A., Reid, M. J., et al. 2011, *ApJS*, 194, 25
- Kerr, F. J. 1967, *Radio Astronomy and the Galactic System*, 31, 239
- Kettenis, M., van Langevelde, H. J., Reynolds, C., & Cotton, B. 2006, *Astronomical Data Analysis Software and Systems XV*, 351, 497
- Jackson, J. M., Rathborne, J. M., Shah, R. Y., et al. 2006, *ApJS*, 163, 145
- Liu, H. B., Zhang, Q., & Ho, P. T. P. 2011, *ApJ*, 729, 100
- Lockman, F. J. 1980, *ApJ*, 241, 200
- Marshall, D. J., Fux, R., Robin, A. C., & Reyl e, C. 2008, *A&A*, 477, L21
- Morris, M., & Serabyn, E. 1996, *ARA&A*, 34, 645
- Peters, W. L., III 1975, *ApJ*, 195, 617
- Petrov, L., Kovalev, Y. Y., Fomalont, E., & Gordon, D. 2005, *AJ*, 129, 1163
- Reid, M. J., Menten, K. M., Brunthaler, A., Zheng, X. W., Moscadelli, L., & Xu, Y. 2009a, *ApJ*, 693, 397
- Reid, M. J., et al. 2009, *ApJ*, 700, 137
- Reid, M. J. 2013, *IAU Symposium*, 289, 188
- Roberts, W. W., Jr., Huntley, J. M., & van Albada, G. D. 1979, *ApJ*, 233, 67
- Rodr guez-Fernandez, N. J., & Combes, F. 2008, *A&A*, 489, 115
- Sanna, A., Reid, M. J., Moscadelli, L., et al. 2009, *ApJ*, 706, 464
- Sanna, A., Moscadelli, L., Cesaroni, R., Tarchi, A., Furuya, R. S., & Goddi, C. 2010, *A&A*, 517, A71



- Sato, M., Reid, M. J., Brunthaler, A., & Menten, K. M. 2010, *ApJ*, 720, 1055
- Sewilo, M., Watson, C., Araya, E., et al. 2004, *ApJS*, 154, 553
- Schönrich, R., Binney, J., & Dehnen, W. 2010, *MNRAS*, 403, 1829
- Sofue, Y., Tutui, Y., Honma, M., et al. 1999, *ApJ*, 523, 136
- Steiman-Cameron, T. Y., Wolfire, M., & Hollenbach, D. 2010, *ApJ*, 722, 1460
- Taylor, J. H., & Cordes, J. M. 1993, *ApJ*, 411, 674
- Vallée, J. P. 2008, *AJ*, 135, 1301
- van Albada, T. S., & Sanders, R. H. 1982, *MNRAS*, 201, 303
- van der Kruit, P. C. 1971, *A&A*, 13, 405
- Wilkinson, P. N., Browne, I. W. A., Patnaik, A. R., Wrobel, J. M., & Sorathia, B. 1998, *MNRAS*, 300, 790
- Wilson, T. L. 1974, *A&A*, 31, 83
- Xu, Y., Li, J. J., Reid, M. J., et al. 2013, *ApJ*, 769, 15

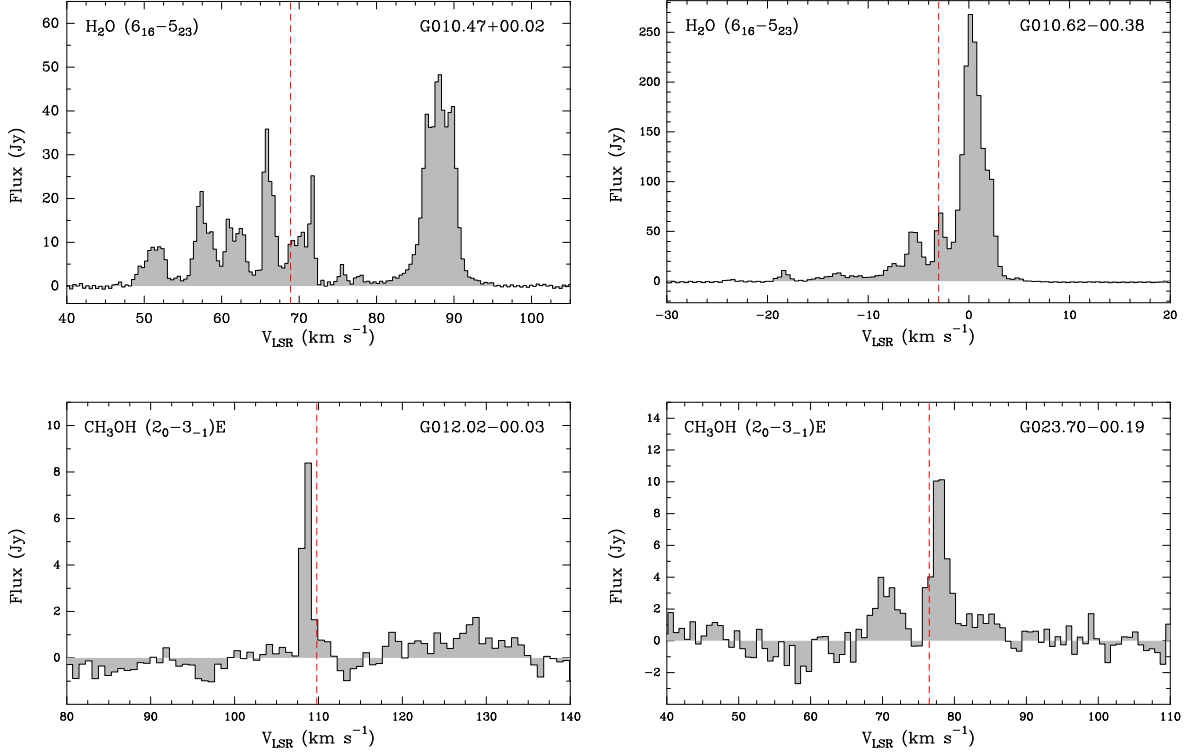


Fig. 1.— Total-power (Stokes I) spectra of the maser emission from the first epoch data for the inner Galaxy sources. These profiles were obtained by averaging the total-power spectra of all VLBA antennas with the task POSSM of AIPS and removing the baseline within the CLASS package of GILDAS (<http://www.iram.fr/IRAMFR/GILDAS>). Each dashed vertical line marks the systemic velocity ( $V_{\text{sys}}$ ) of the large-scale molecular cloud hosting the star-forming region (see Table 4 and Appendix A). See the electronic edition of the Journal for a color version of this figure.

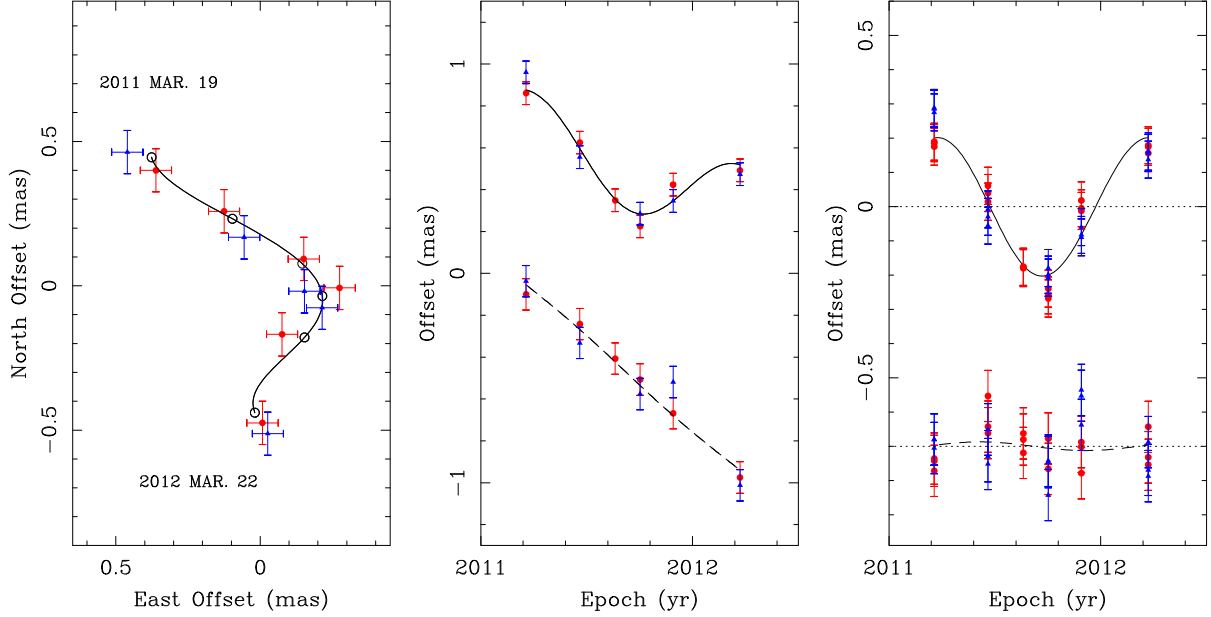


Fig. 2.— Results of the “combined” parallax fit for G010.62–00.38. *Left Panel:* Sky projected motion of a single maser spot at  $+1.0 \text{ km s}^{-1}$  with respect to J1751–1950 (red circles) and J1821–2110 (blue triangles) with first and last epochs labeled. The empty circles and the line show the best-fit position offsets and the trajectory, respectively. *Middle Panel:* The position offsets of the maser at  $+1.0 \text{ km s}^{-1}$  along the east and north directions versus time. The best-fit model in east and north directions are shown as continuous and dashed lines, respectively. *Right Panel:* Same as the middle panel but with fitted proper motions subtracted (i.e. parallax curve) and all maser spots measurements drawn for each QSO (3 maser spots and 2 QSOs). The north offset data have been shifted for clarity. See the electronic edition of the Journal for a color version of this figure.

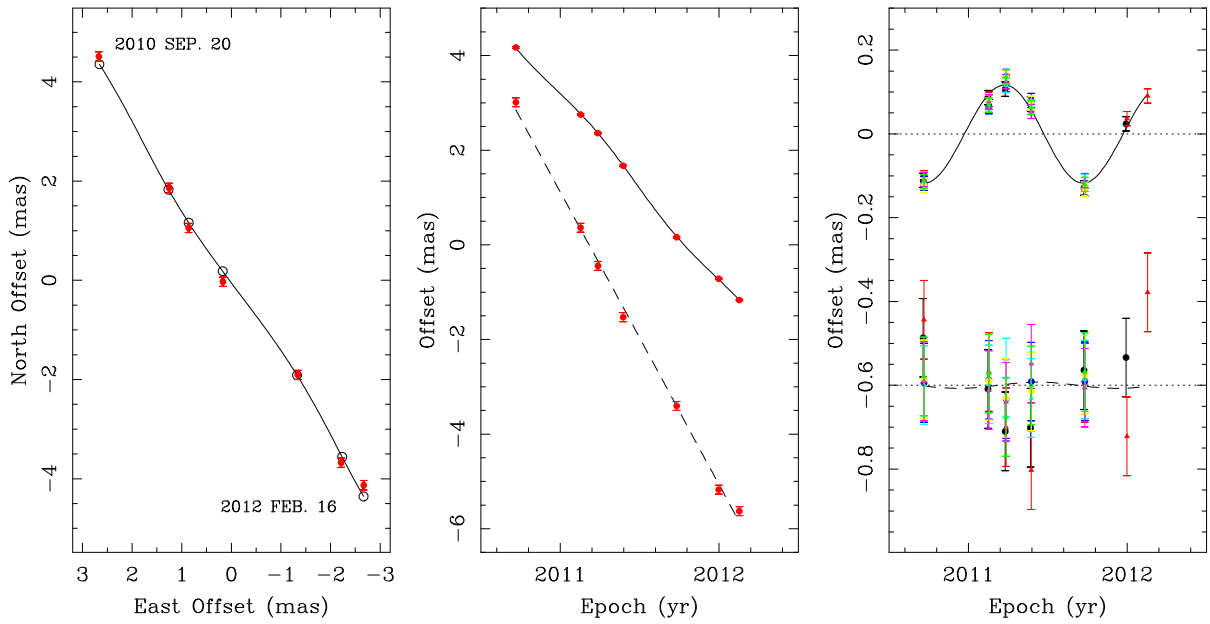


Fig. 3.— Results of the “combined” parallax fit for G010.47+00.02. Similar to Figure 2 with positions for a maser spot at  $68.0 \text{ km s}^{-1}$  (red circles), which lasted for the higher number of epochs, measured relative to J1751–1950 (left and middle panels). For the parallax curve (right panel), all maser spots are drawn with different colors (7 maser spots and 1 QSO). See the electronic edition of the Journal for a color version of this figure.

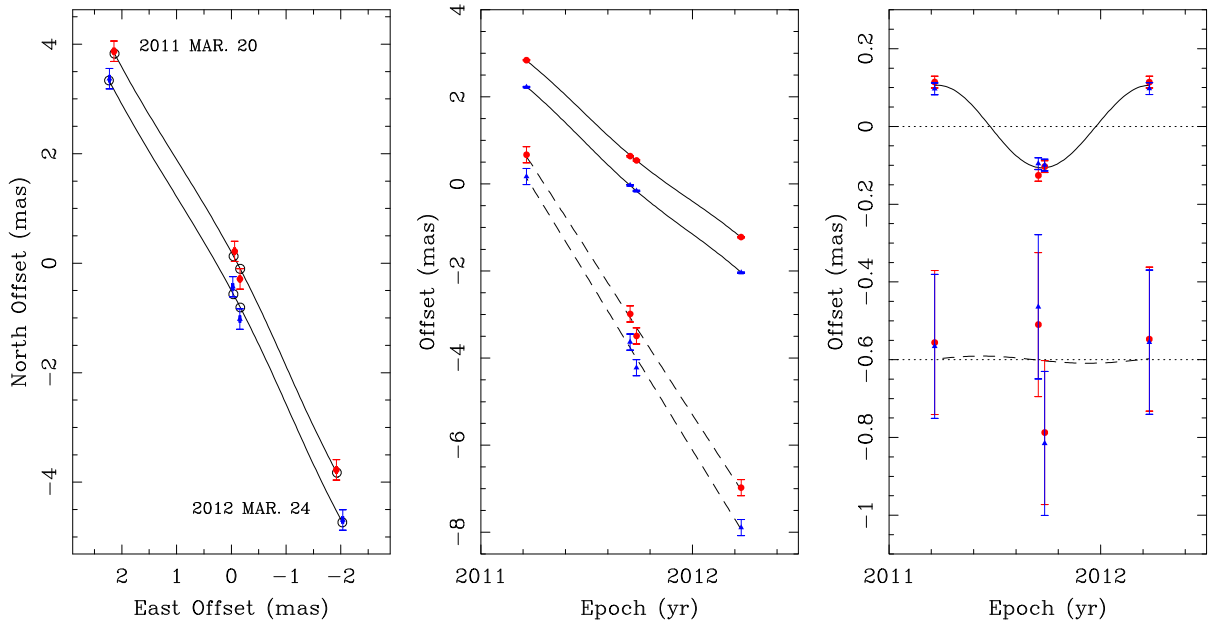


Fig. 4.— Results of the “combined” parallax fit for G012.02–00.03. Similar to Figure 2 with maser positions for spots at  $+108.0$  (blue triangles) and  $+108.8 \text{ km s}^{-1}$  (red circles) measured relative to J1808–1822 (2 maser spots and 1 QSO). See the electronic edition of the Journal for a color version of this figure.

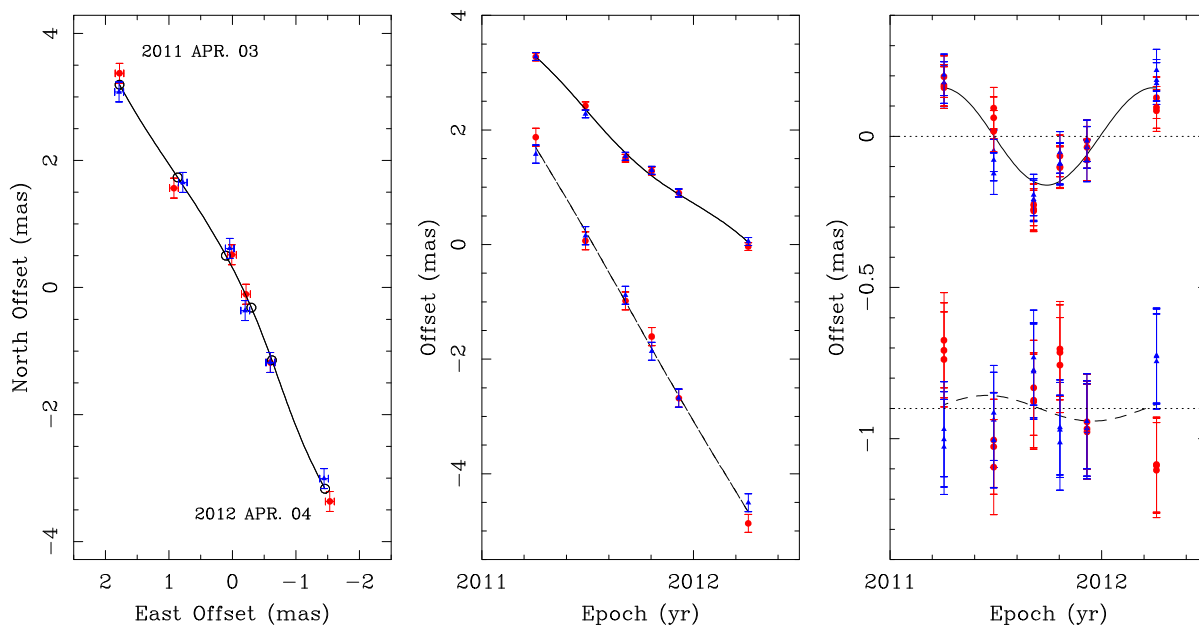


Fig. 5.— Results of the “combined” parallax fit for G023.70–00.19. Similar to Figure 2 with maser positions for spot at  $+79.0 \text{ km s}^{-1}$  with respect to J1825–0737 (red circles) and J1846–0651 (blue triangles), and all maser spots drawn for the parallax curve in the right panel (3 maser spots and 2 QSOs). See the electronic edition of the Journal for a color version of this figure.

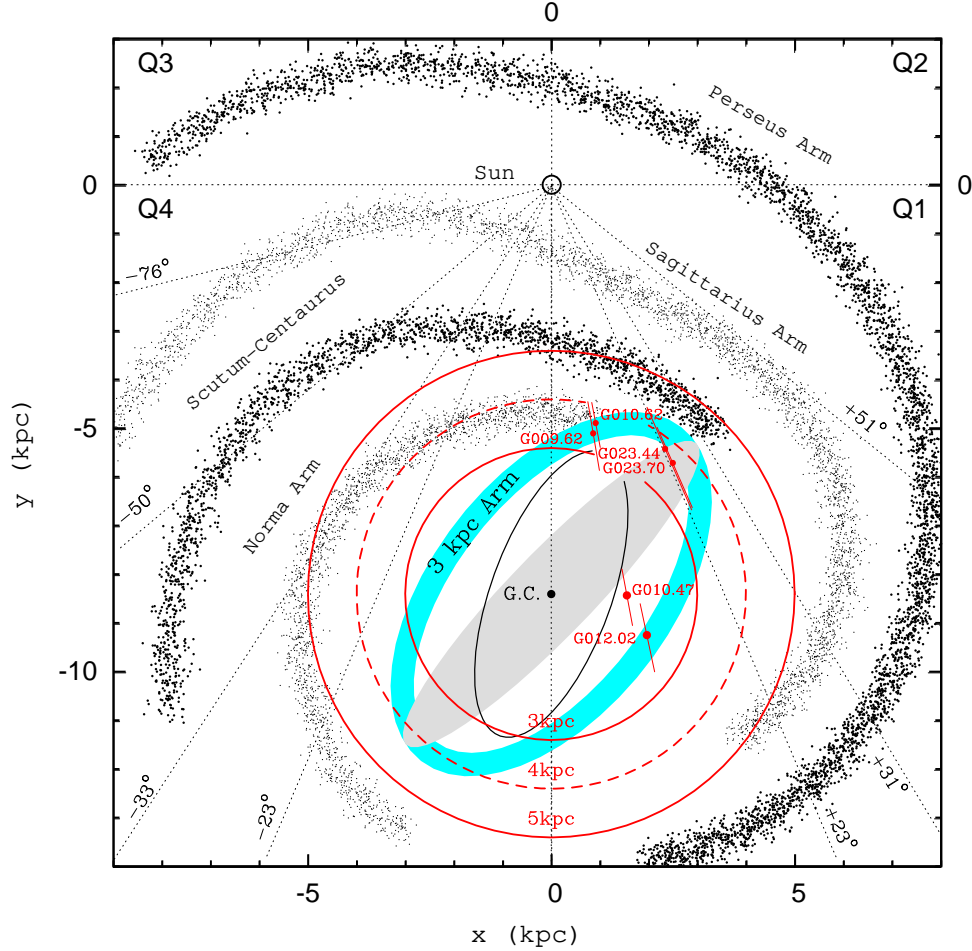


Fig. 6.— Schematic view of the spiral arms of the Milky Way across the four Galactic quadrants after Taylor & Cordes (1993) with updates. The best-value of  $R_0 = 8.38$  kpc from Reid (2013) is assumed. The location of the Galactic bar (i.e., the bulge) and the central “long” bar as from Churchwell et al. (2009) are also reported as an open and light-grey ellipsoids, respectively. Positions of the inner Milky Way sources from Table 4 are labeled as well (red dots) together with error bars. Dotted lines drawn from the Sun position across the first and fourth Galactic quadrants mark the tangents to major spiral arms as from Vallée (2008). The near 3 kpc arm tangents at  $\pm 23^\circ$  are adopted following Dame & Thaddeus (2008). The azure ellipsoid outlines the locus of the 3 kpc arms following the best fit model to the  $\ell$ - $v$  position of 6.7 GHz masers by Green et al. (2011), with a total width of 0.5 kpc. See the electronic edition of the Journal for a color version of this figure.

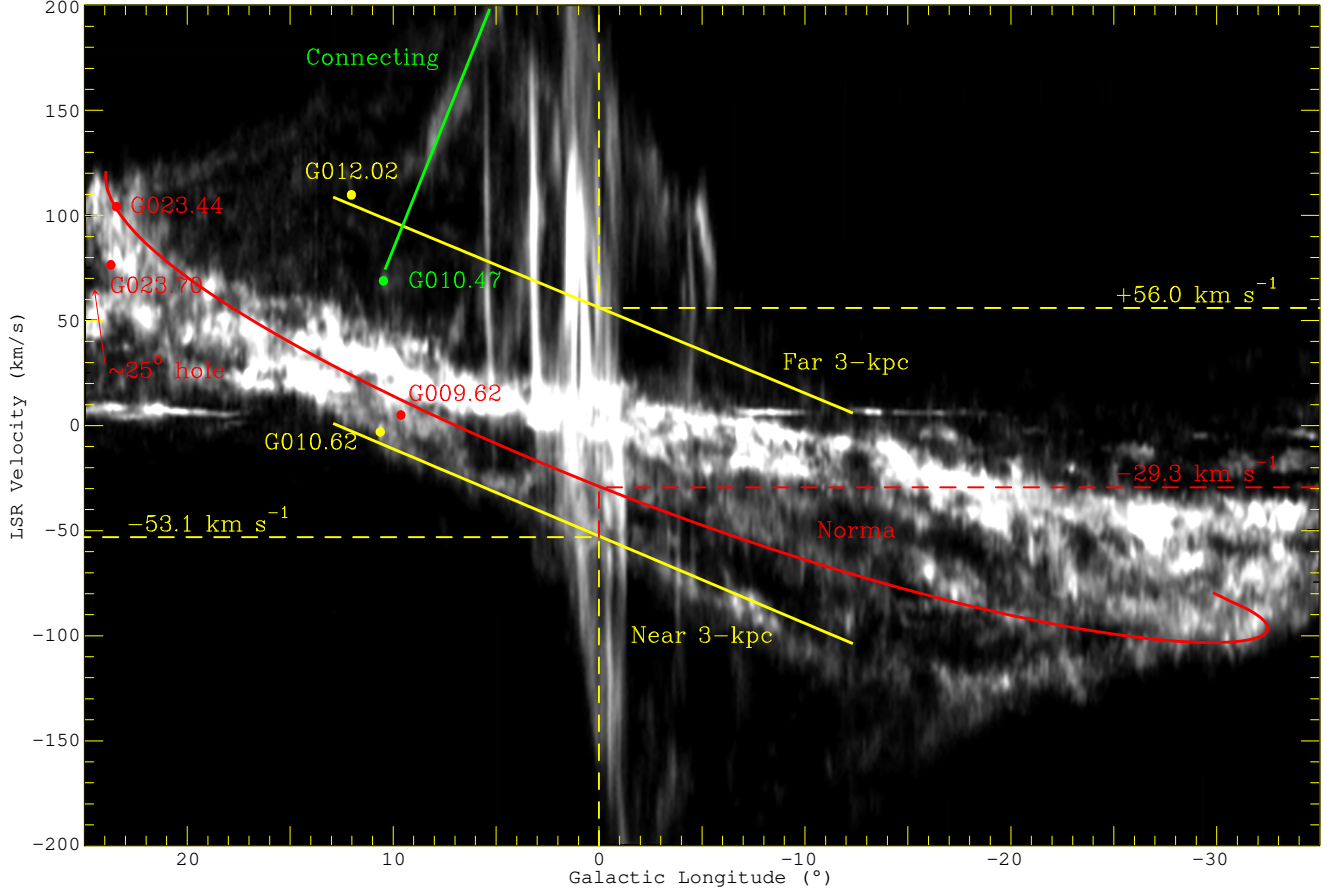


Fig. 7.— Longitude-velocity diagram of the CO emission integrated within  $-1^\circ \leq b \leq +1^\circ$  from Dame et al. (2001). The gray scale is CO intensity ranging from 0 (black) to 4 K arcdeg (white). Lines draw the  $\ell$ - $v$  positions of gas associated with the inner arms: the yellow lines mark the near and far 3 kpc arms from Dame & Thaddeus (2008), the green line marks the Connecting arm (e.g., Fux 1999, his Figure 1) and the red line marks a best-guess for the Norma arm locus (see Section 3.1). The expanding velocity components of the Norma and 3 kpc arms at  $\ell = 0^\circ$  are marked for each fit as well. Positions of star-forming regions listed in Table 4 are plotted and color-coded according to the associated arms, together with the position of the “gas hole” near  $\ell \sim 25^\circ$  separating the Norma and Scutum-Centaurus arms (Cohen et al. 1980, their Figure 2). See the electronic edition of the Journal for a color version of this figure.



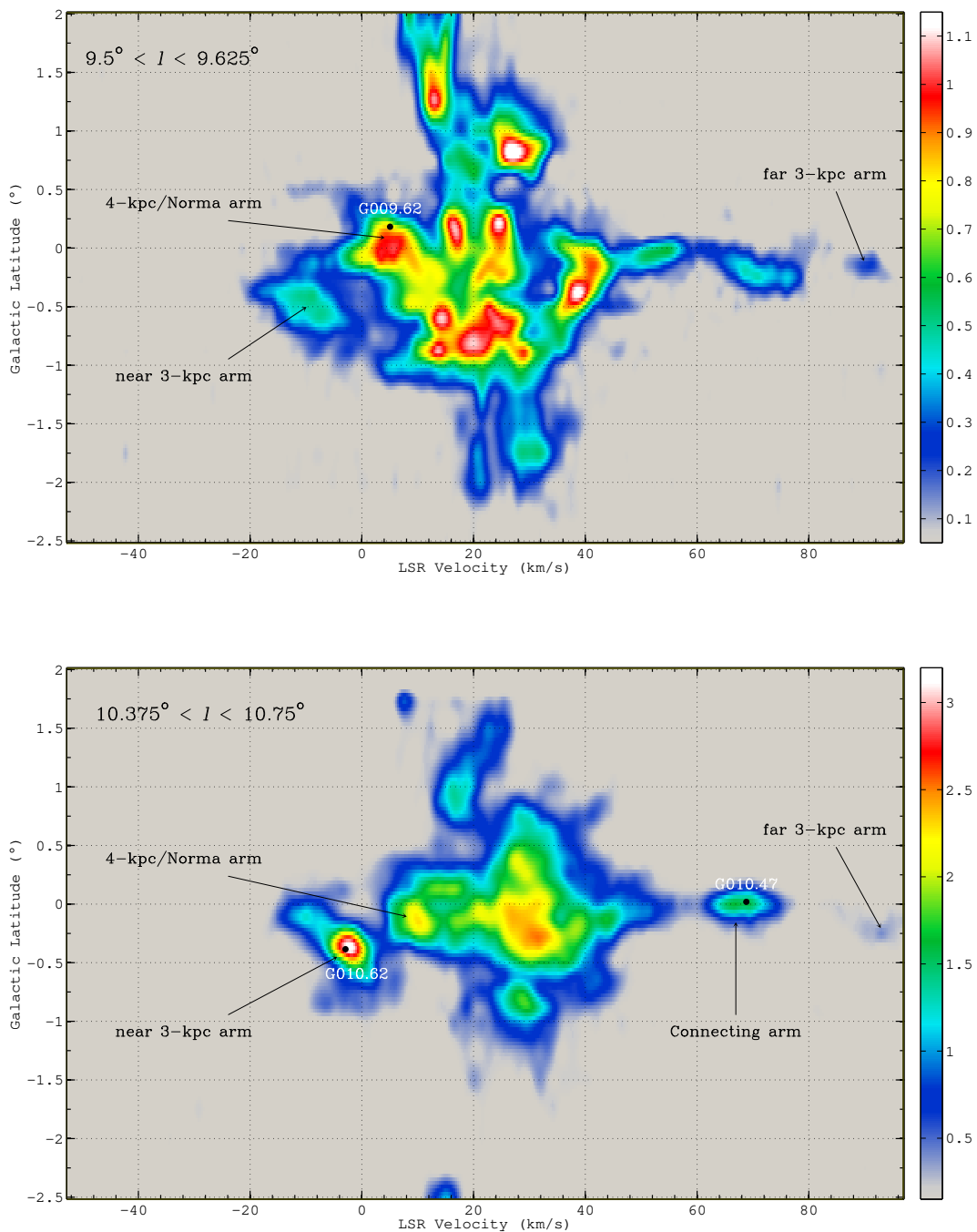


Fig. 8.— Latitude-velocity diagrams of the CO emission integrated within the range of longitudes where the Norma and near 3 kpc arms intersect in Figure 6. CO data are from the 1.2 m Cerro Tololo survey of Bitran et al. (1997). The CO emission was integrated within the ranges of Galactic longitudes indicated in the upper left corner of each panel. The color scale on the right-hand side of each panel corresponds to the CO intensity range in K arcdeg. Positions of prominent arms in the inner Milky Way are labeled in each panel together with the associated sources according to Table 4. See the electronic edition of the Journal for a color version of this figure.

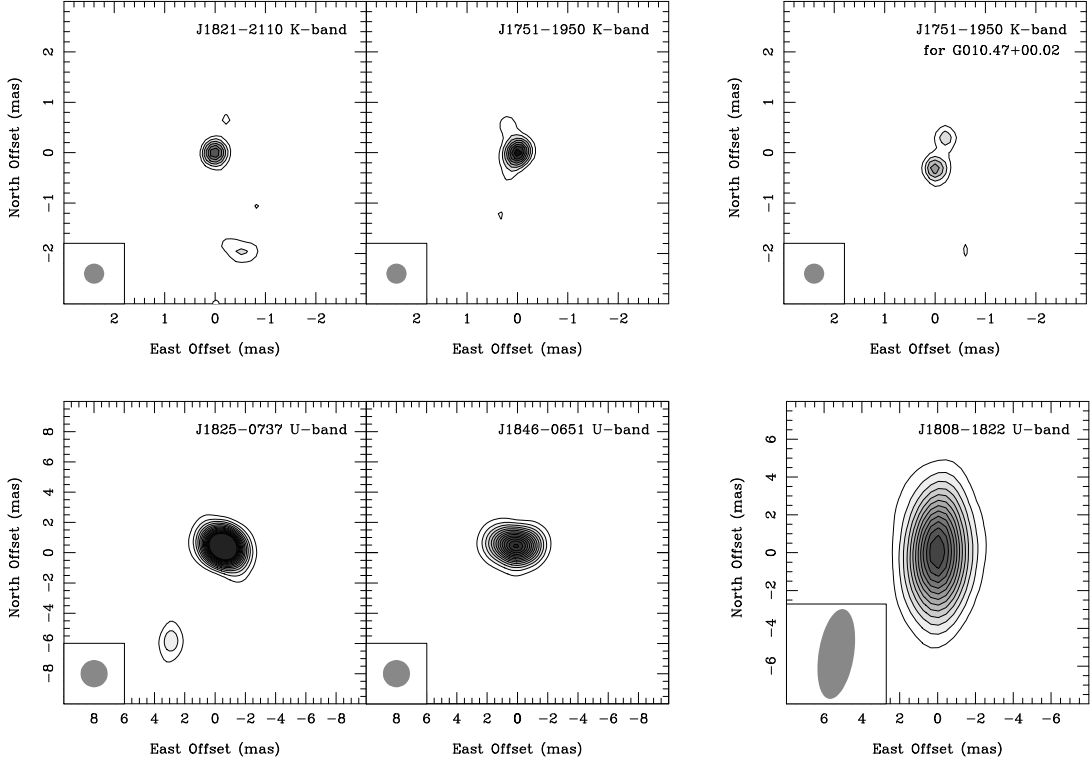


Fig. 9.— Images of the background continuum sources in K and U bands near the target masers used for parallax purposes. All images are from the first epoch observations (see Table 1). Source names are indicated in the upper right corner and restoring beams are drawn in the lower left corner of each panel. Contour levels start at  $3\sigma$  by steps of  $2\sigma$  and  $3\sigma$  for the K and U-band calibrators, respectively (see Table 2). K-band calibrators for G010.62–00.38 and G010.47+00.02 were imaged with an HPBW of 0.4 mas (round), U-band calibrators for G023.70–00.19 were imaged with an HPBW of 1.8 mas (round), and the calibrator for G012.02–00.03 was imaged with a natural restoring beam.

Table 1. Observation Information

Exp. code:	BR145M	BR145O	BR145Q	BR145U
Target	G010.62–00.38	G023.70–00.19	G012.02–00.03	G010.47+00.02
Maser line	22.2 GHz H <sub>2</sub> O	12.2 GHz CH <sub>3</sub> OH	12.2 GHz CH <sub>3</sub> OH	22.2 GHz H <sub>2</sub> O
V <sub>LSR</sub> (km s <sup>-1</sup> )	1.0	79.0	108.0	65.0
prep.survey	BR145AL	BR145AK	BR145AH	BR145AW
Epoch:				
1	2011 MAR 19	2011 APR 03	2011 MAR 20	2010 SEP 20
2	2011 JUN 20	2011 JUN 28	2011 SEP 15	2010 DEC 23
3	2011 AUG 20	2011 SEP 05	2011 SEP 26	2011 FEB 16
4	2011 OCT 02	2011 OCT 20	2012 MAR 24	2011 MAR 28
5	2011 NOV 28	2011 DEC 06		2011 MAY 25
6	2012 MAR 22	2012 APR 04		2011 SEP 25
7				2011 DEC 31
8				2012 FEB 16
9				2012 MAR 26
10				2012 MAY 13
11				2012 SEP 23

Note. — Scheduling information for the VLBA observations.

Table 2. Source Information

Source	R.A. (J2000) (h m s)	Decl. (J2000) (° ' ")	$\theta_{\text{sep}}$ (°)	P.A. (°)	HPBW mas $\times$ mas at °	$F_{\text{peak}}$ (Jy beam <sup>-1</sup> )	Image rms (Jy beam <sup>-1</sup> )	$V_{\text{LSR}}$ (km s <sup>-1</sup> )
<b>G010.62–00.38</b>	18 10 28.5629	–19 55 48.738			$1.2 \times 0.6$ at $-1.8^\circ$	42.94	0.05	–2.8
J1808–1822	18 08 55.5154	–18 22 53.396	1.6	–13	$1.2 \times 0.6$ at $-2.0^\circ$	0.011	0.001	
J1821–2110	18 21 05.4692	–21 10 45.262	2.8	+117	$1.3 \times 0.6$ at $-1.3^\circ$	0.016	0.001	
J1751–1950 <sup>a</sup>	17 51 41.3438	–19 50 47.506	4.4	–90	$1.2 \times 0.8$ at $+4.4^\circ$	0.049	0.002	
J1809–1520	18 09 10.2094	–15 20 09.699	4.6	–4	$1.2 \times 0.6$ at $-2.3^\circ$	0.013	0.001	
<b>G010.47+00.02</b>	18 08 38.2302	–19 51 50.253			$1.3 \times 0.4$ at $-17.1^\circ$	22.55	0.04	+89.9
J1808–1822	18 08 55.5154	–18 22 53.396	1.5	+4	$1.0 \times 0.4$ at $-12.0^\circ$	0.006	0.001	
J1751–1950 <sup>a</sup>	17 51 41.3438	–19 50 47.506	3.2	–90	$1.3 \times 0.4$ at $-9.8^\circ$	0.009	0.001	
J1821–2110	18 21 05.4692	–21 10 45.262	4.0	+66	$1.2 \times 0.4$ at $-9.4^\circ$	0.006	0.001	
<b>G012.02–00.03</b>	18 12 01.8455	–18 31 55.759			$2.3 \times 1.1$ at $-0.7^\circ$	2.37	0.01	+108.8
J1808–1822	18 08 55.5154	–18 22 53.396	0.8	–78	$4.8 \times 1.9$ at $-9.2^\circ$	0.039	0.001	
J1809–1520	18 09 10.2094	–15 20 09.699	3.3	–12	$3.3 \times 1.8$ at $+6.9^\circ$	0.039	0.001	
J1825–1718 <sup>a</sup>	18 25 36.5323	–17 18 49.848	3.4	+70	$4.8 \times 1.9$ at $-8.4^\circ$	0.174	0.001	
J1751–1950 <sup>a</sup>	17 51 41.3438	–19 50 47.506	5.0	–106	$5.2 \times 2.0$ at $-7.6^\circ$	0.068	0.001	
<b>G023.70–00.19</b>	18 35 12.3645	–08 17 39.396			$2.9 \times 1.3$ at $-5.2^\circ$	3.99	0.02	+77.5
J1825–0737 <sup>a</sup>	18 25 37.6096	–07 37 30.013	2.5	–74	$3.3 \times 1.8$ at $+3.8^\circ$	0.315	0.003	
J1846–0651 <sup>a</sup>	18 46 06.3002	–06 51 27.748	3.1	+63	$3.3 \times 1.8$ at $+2.2^\circ$	0.043	0.001	
J1821–0502 <sup>a</sup>	18 21 11.8094	–05 02 20.087	4.8	–47	$3.2 \times 1.8$ at $+11.7^\circ$	0.190	0.002	

Note. — Positions and source properties for the target maser and the QSO calibrators from the first epoch data. The peak position of the phase-reference maser channels No. 138, 70, 128, and 131 (for sources from the top to the bottom, respectively) were calibrated with the ICRF sources and are accurate to within  $\pm 2$  mas. For calibrators, we report positions used at the VLBA correlator. Angular offsets ( $\theta_{\text{sep}}$ ) and position angles (P.A.) east of north relative to the maser source are indicated in columns 4 and 5. Columns 6, 7, and 8 give the natural restoring beam sizes (HPBW), the peak intensities ( $F_{\text{peak}}$ ), and image rms noise of the phase-reference maser channels (at  $V_{\text{LSR}}$ ), K-band, and U-band background sources.

<sup>a</sup>Sources belonging to the ICRF catalog.

Table 3. Parallax & Proper Motion Fits

Maser $V_{\text{LSR}}$ ( $\text{km s}^{-1}$ )	$\Delta x$ & $\Delta y$ (mas)	Background Source	Parallax (mas)	D (kpc)	$\mu_x$ ( $\text{mas yr}^{-1}$ )	$\mu_y$ ( $\text{mas yr}^{-1}$ )
<b>G010.47+00.02</b>						
+75.5	+3.6; -329.1	J1751-1950	$0.116 \pm 0.007$		$-4.029 \pm 0.014$	$-6.515 \pm 0.119$
+68.0	-46.0; +68.8	J1751-1950	$0.115 \pm 0.007$		$-3.933 \pm 0.012$	$-6.187 \pm 0.146$
+67.1	-66.7; +16.4	J1751-1950	$0.122 \pm 0.015$		$-3.890 \pm 0.039$	$-6.384 \pm 0.036$
+67.1	-65.3; +69.4	J1751-1950	$0.110 \pm 0.007$		$-3.959 \pm 0.019$	$-6.855 \pm 0.040$
+62.9	-66.7; +89.5	J1751-1950	$0.125 \pm 0.010$		$-4.044 \pm 0.028$	$-6.729 \pm 0.049$
+59.5	+33.3; +57.7	J1751-1950	$0.111 \pm 0.007$		$-3.533 \pm 0.018$	$-6.402 \pm 0.056$
+59.5	-92.1; -136.3	J1751-1950	$0.117 \pm 0.011$		$-3.787 \pm 0.030$	$-6.479 \pm 0.082$
+75.5		Combined	$0.117 \pm 0.008$	$8.55^{+0.63}_{-0.55}$	$-4.028 \pm 0.016$	$-6.514 \pm 0.089$
+68.0					$-3.932 \pm 0.013$	$-6.185 \pm 0.073$
+67.1					$-3.890 \pm 0.022$	$-6.385 \pm 0.122$
+67.1					$-3.959 \pm 0.022$	$-6.855 \pm 0.122$
+62.9					$-4.044 \pm 0.022$	$-6.729 \pm 0.122$
+59.5					$-3.534 \pm 0.022$	$-6.402 \pm 0.122$
+59.5					$-3.788 \pm 0.022$	$-6.480 \pm 0.122$
<b>Best-value for the Secular proper motion of G010.47+00.02</b>						
			$0.117 \pm 0.008$	$8.55^{+0.63}_{-0.55}$	$-3.860 \pm 0.015$	$-6.403 \pm 0.076$
<b>G010.62-00.38</b>						
-14.2	+607.0; -605.1	J1751-1950	$0.191 \pm 0.034$		$-0.632 \pm 0.084$	$-0.503 \pm 0.122$
-14.2		J1821-2110	$0.200 \pm 0.040$			
-1.1	+386.9; -247.3	J1751-1950	$0.202 \pm 0.034$		$-0.427 \pm 0.084$	$-1.474 \pm 0.084$
-1.1		J1821-2110	$0.216 \pm 0.026$			
+1.0	+324.8; -194.5	J1751-1950	$0.200 \pm 0.030$		$-0.355 \pm 0.075$	$-0.876 \pm 0.053$
+1.0		J1821-2110	$0.213 \pm 0.032$			
-14.2		Combined	$0.202 \pm 0.019$	$4.95^{+0.51}_{-0.43}$	$-0.632 \pm 0.084$	$-0.503 \pm 0.122$
-1.1					$-0.427 \pm 0.084$	$-1.474 \pm 0.084$
+1.0					$-0.355 \pm 0.075$	$-0.876 \pm 0.053$
<b>Best-value for the Secular proper motion of G010.62-00.38</b>						
			$0.202 \pm 0.019$	$4.95^{+0.51}_{-0.43}$	$-0.366 \pm 0.081$	$-0.600 \pm 0.055$
<b>G012.02-00.03</b>						
+108.0	+0.6; +1.0	J1808-1822	$0.098 \pm 0.001$		$-4.205 \pm 0.003$	$-7.963 \pm 0.349$
+108.8	0.0; 0.0	J1808-1822	$0.115 \pm 0.008$		$-4.008 \pm 0.023$	$-7.551 \pm 0.279$
+108.0		Combined	$0.106 \pm 0.008$	$9.43^{+0.77}_{-0.66}$	$-4.205 \pm 0.022$	$-7.963 \pm 0.265$
+108.8					$-4.008 \pm 0.022$	$-7.551 \pm 0.265$
<b>G023.70-00.19</b>						
+77.5	0.0; 0.0	J1825-0737	$0.163 \pm 0.038$		$-3.226 \pm 0.096$	$-6.704 \pm 0.224$
+77.5		J1846-0651	$0.187 \pm 0.028$		$-3.100 \pm 0.071$	$-6.237 \pm 0.115$

Table 3—Continued

Maser $V_{\text{LSR}}$ ( $\text{km s}^{-1}$ )	$\Delta x$ & $\Delta y$ (mas)	Background Source	Parallax (mas)	D (kpc)	$\mu_x$ ( $\text{mas yr}^{-1}$ )	$\mu_y$ ( $\text{mas yr}^{-1}$ )
+76.7	+2.7; -21.5	J1825-0737	$0.154 \pm 0.034$		$-3.299 \pm 0.084$	$-6.518 \pm 0.256$
+76.7		J1846-0651	$0.173 \pm 0.041$		$-3.171 \pm 0.103$	$-6.046 \pm 0.167$
+79.0	+1.6; -2.5	J1825-0737	$0.136 \pm 0.041$		$-3.288 \pm 0.103$	$-6.577 \pm 0.231$
+79.0		J1846-0651	$0.161 \pm 0.036$		$-3.159 \pm 0.090$	$-6.104 \pm 0.116$
+77.5		Combined	$0.161 \pm 0.024$	$6.21^{+1.0}_{-0.80}$	$-3.164 \pm 0.059$	$-6.474 \pm 0.136$
+76.7					$-3.235 \pm 0.059$	$-6.283 \pm 0.136$
+79.0					$-3.223 \pm 0.059$	$-6.338 \pm 0.136$

Note. — Columns 1 and 2 report the LSR velocity and the offset positions of the reference maser spots, respectively, with respect to the phase-reference maser channels in Table 2. Column 3 indicates the background sources whose data were used to model the relative proper motion of the maser for the parallax fit; column 4 and 5 report the fitted parallax and distance; columns 6 and 7 give the fitted proper motions along the east and north directions, respectively. Combined fit used a single parallax parameter for the maser spots relative to the QSOs. Quoted uncertainties for individual parallax fits are from the formal fitting uncertainty. The Secular proper motion of G010.47+00.02 and G010.62-00.38 was obtained by the combined fit value corrected for the internal proper motions of the overall H<sub>2</sub>O maser distribution.

Table 4. Galactic motion of sources in the inner Milky Way

Source	$\ell$ (deg)	b (deg)	$V_{\text{LSR}}$ (km s $^{-1}$ )	D (kpc)	R (kpc)	$U_s^{\text{G.C.}}$ (km s $^{-1}$ )	$V_s^{\text{G.C.}}$ (km s $^{-1}$ )	$W_s^{\text{G.C.}}$ (km s $^{-1}$ )	Ref.	Arm
G009.62+00.19	9.621	+0.196	$+5.0 \pm 3.1$	$5.15^{+0.77}_{-0.66}$	$3.4^{+0.6}_{-0.7}$	$-36.1 \pm 16.7$	$+191.9 \pm 15.1$	$-10.1 \pm 4.1$	1	Norma
G010.47+00.02	10.472	+0.027	$+68.9 \pm 4.5$	$8.55^{+0.63}_{-0.55}$	$1.6^{+0.2}_{-0.1}$	$+30.3 \pm 21.5$	$+121.7 \pm 15.8$	$+18.2 \pm 1.8$	2	Connecting
G010.62–00.38 (W31)	10.624	–0.383	$-3.0 \pm 2.7$	$4.95^{+0.51}_{-0.43}$	$3.6^{+0.4}_{-0.4}$	$-60.8 \pm 14.4$	$+228.2 \pm 6.7$	$+8.1 \pm 1.8$	2	near 3 kpc
G012.02–00.03	12.025	–0.031	$+109.8 \pm 2.4$	$9.43^{+0.77}_{-0.66}$	$2.1^{+0.5}_{-0.3}$	$+25.5 \pm 32.7$	$+215.0 \pm 26.8$	$+1.5 \pm 5.8$	2	far 3 kpc
G023.44–00.18	23.440	–0.182	$+104.2 \pm 4.3$	$5.88^{+1.37}_{-0.93}$	$3.8^{+0.5}_{-0.4}$	$+4.7 \pm 42.7$	$+225.4 \pm 18.1$	$+2.0 \pm 3.1$	3	Norma
G023.70–00.19	23.707	–0.198	$+76.5 \pm 10$	$6.21^{+1.0}_{-0.80}$	$3.7^{+0.4}_{-0.3}$	$+51.4 \pm 15.5$	$+167.1 \pm 12.0$	$+4.6 \pm 2.6$	2	Norma

Note. — Proper motion of sources that belong to the inner Milky Way with respect to a reference frame joined with the Galactic center (see Section 3). For converting the heliocentric measurements to the Galactic center reference frame, we considered the best estimates of  $R_0 = 8.38$  kpc and  $\Theta_0 = 243$  km s $^{-1}$  given in Reid (2013) and the updated values of the Solar motion in Schönrich et al. (2010). Column 4 gives the LSR velocity of the regions assumed in the calculation, as inferred from the CS(2–1) line survey by Bronfman et al. (1996) with the exception of G010.62–00.38 and G023.70–00.19 (see Appendix A). Columns 5 and 6 report the heliocentric and projected Galactocentric distance of each source, respectively. Columns 7, 8, and 9 give the velocity components toward the Galactic center, in the direction of Galactic rotation, and toward the North Galactic Pole, respectively. Column 10 lists the reference papers for the trigonometric parallax measurements: (1) Sanna et al. (2009); (2) this work; (3) Brunthaler et al. (2009). Last column lists the Galactic arms associated with the HMSFRs as presented in Section 3.1.